European Conference on Computational Fluid Dynamics
ECCOMAS CFD 2006
P. Wesseling, E. Oñate and J. Périaux (Eds)

ADAPTIVE SONIC BOOM SENSITIVITY ANALYSIS

Frédéric Alauzet*

*INRIA, projet Gamma
Domaine de Voluceau - Rocquencourt
B.P.105, 78135 Le Chesnay, France
e-mail: frederic.alauzet@inria.fr
web page: http://www-rocq.inria.fr/who/Frederic.Alauzet/

Key words: Sonic Boom, Computational Fluid Dynamics, Mesh Adaptation, Waveform Parameter Method, Finite Volume Method, Supersonic Jet.

Abstract. *This paper presents an accurate approach to simulate the sonic boom of a supersonic aircraft. The near field flow is modeled by the conservative Euler equations and is solved using a finite volume approach on adapted unstructured tetrahedral meshes. Then, from the CFD solution, the pressure distribution under the aircraft is extracted and used to set up the initial conditions of the propagation algorithm in the far field. The pressure distribution is propagated down to the ground in order to obtain the sonic boom signature using a ray tracing algorithm based upon the Thomas waveform parameter method. In this study, a sonic boom sensitivity analysis on the SSBJ geometry provided by Dassault Aviation is carried out.*

1 INTRODUCTION

Nowadays, an accurate prediction of the sonic boom is crucial in designing low sonic boom aircraft configurations, in order to respect environmental constraints. This paper proposes an approach to predict the sonic boom issued from a supersonic aircraft, the SuperSonic Business Jet (SSBJ) designed by Dassault Aviation.

Developing a sonic boom model requires the coupling of CFD equations for the near field simulation with waves propagation equations for the far field. Thus, the resolution is performed in two steps, Figure 1. Firstly, the flow close to the aircraft, named aerodynamic near field region, is computed. The near field flow is modeled by the conservative Euler equations for gas dynamic and is solved using a finite volume approach on adapted unstructured tetrahedral meshes [5]. Then, from the CFD solution, the pressure distribution under the aircraft is extracted and used to set up the initial conditions of the propagation algorithm in the far field. The pressure distribution is propagated down to the ground in order to obtain the sonic boom signature using a ray tracing algorithm based upon the Thomas waveform parameter method [11].

Nevertheless, the modeled flow in the near field is three-dimensional and non linear in nature whereas the propagation is a linear one-dimensional model. Thus, the near field solution must be locally axi-symmetric where the pressure distribution is extracted to ensure a valid coupling. This is a necessary condition to take all the elements of the aircraft geometry (body, wings,...) into account. Therefore, a precise near field solution far from the aircraft is needed to obtain an accurate prediction of the sonic boom. To this end, we propose using a mesh adaptation approach [6].

In the following sections, we present the proposed appraoch. Section 2, we describe the Finite Volume scheme used to compute near field region flow. Section 3, we recall the mesh adaptation algorithm and we briefly review the main stages of the adaptation procedure. The ray tracing algorithm based upon the Thomas waveform parameter method is described in Section 4. Then, the coupling between the CFD and the propagation code is clarified in Section 5.

In this study, a sonic boom sensitivity analysis on the SSBJ geometry is carried out in Section 6. More precisely, we point out the impact of the anisotropic mesh adaptation to compute an accurate near field signature and the choice of near field solutions on the sonic boom prediction is analyzed.

2 CFD MODELING

The near field flow around the aircraft is modeled by the Euler equations. Assuming that the gas is perfect, non viscous and that there is no thermal diffusion, the Euler equations for mass, momentum and energy conservation read:

$$\left\{ \begin{array}{rcl} \dfrac{\partial \rho}{\partial t} + \nabla.\,(\rho \vec{U}) & = & 0\,, \\ \dfrac{\partial (\rho \vec{U})}{\partial t} + \nabla.\,(\rho \vec{U} \otimes \vec{U}) + \nabla p & = & 0\,, \\ \dfrac{\partial (\rho E)}{\partial t} + \nabla.\,((\rho E + p)\vec{U}) & = & 0\,, \end{array} \right.$$

where ρ denotes the density, $\vec{U}$ the velocity vector, $E = T + \frac{\|\vec{U}\|^2}{2}$ the total energy and $p = (\gamma - 1)\rho T$ the pressure with $\gamma \; = \; 1.4$ the ratio of specific heats and T the temperature. These equations could be symbolically rewritten:

$$\frac{\partial W}{\partial t} + \nabla \cdot F(W) = 0\,, \tag{1}$$

where $W \; = \; {}^t(\rho, \rho u, \rho v, \rho w, \rho E)$ is the conservative variables vector and the vector F represents the convective operator.

The Euler system is solved by means of a Finite Volume technique on unstructured tetrahedral meshes using `Wolf` a in-house flow solver.

The proposed scheme is vertex-centered and uses a particular edge-based formulation with upwind elements. This flow solver employs a HLLC approximate Riemann solver to compute numerical fluxes. High-order scheme is derived according to a MUSCL (Monotone Upwind Schemes for Conservation Laws) type method using downstream and upstream tetrahedra. This approach is compatible with vertex-centered and edge-based formulations, allowing rather easy and, importantly, inexpensive higher-order extensions of monotone upwind schemes. The flux integration based on the edges and their corresponding upwind elements (crossed by the edge) is a key-feature in order to preserve the positivity of the density for vertex-centered formulation. The MUSCL type method is combined with a generalization of the Superbee limiter with three entries to guarantee the TVD (Total Variation Diminishing) property to the scheme.

An explicit time stepping algorithm is used by means of a 5-stage, 2-order strong-stability-preserving (SSP) Runge-Kutta scheme that allows us to use a CFL coefficient up to 4. In practice, we consider a CFL equal to 3.5.

2.1 Scheme for convective fluxes

The considered method is a vertex-centred Finite Volume scheme applied to tetrahedral unstructured meshes and uses a particular edge-based formulation with upwind elements introduced in [5]. This formulation consists in associating to each vertex of the mesh a control volume (or finite-volume cell). The dual finite-volume cell mesh is built by the rule of medians. More precisely, each tetrahedron of the mesh is split into four hexahedra constructed around each of its vertex. For a vertex P_i, the hexahedron is defined by the following points: (i) the three middle points of the edges issued from P_i, (ii) the three gravity centers of the faces containing P_i, (iii) the center of gravity of the tetrahedron and (iv) the vertex P_i. The cell C_i of the vertex P_i is the collection of all hexahedra linked to P_i.

The common boundary $\partial C_{ij} = \partial C_i \cap \partial C_j$ between two neighboring cell C_i and C_j is

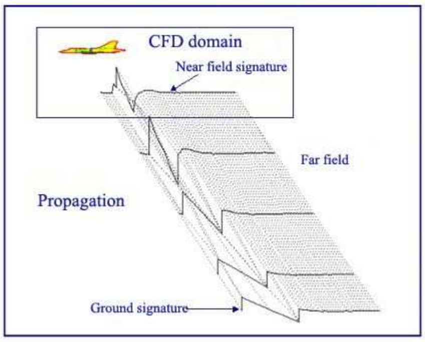

Figure 1: *Sonic boom problem modeling.*

decomposed in several triangular interface facets. Each of this facet has a mid-edge, a face center of gravity and a tetrahedron center of gravity as vertices. An illustration of this construction is two dimensions is shown in Figure 2.

We apply the Finite Volume method to the Euler equations, we get for each finite volume cell C_i:

$$|C_i|\frac{dW_i}{dt} + \int_{\partial C_i} F(W_i)\cdot\vec{n}_i\,d\gamma = 0\,, \tag{2}$$

where W_i is the mean value of the solution W on the cell C_i. The integration of the convective fluxes F is computed by decomposing the cell boundary in facets ∂C_{ij}:

$$\int_{\partial C_i} F(W_i^n)\cdot\vec{n}_i\,d\gamma \;=\sum_{P_j\in\mathcal{V}(P_i)} F|_{I_{ij}}\cdot\int_{\partial C_{ij}}\vec{n}_i\,d\gamma\,,$$

where $\mathcal{V}(P_i)$ is the set of all neighboring vertices of P_i, $\vec{n}_i$ is the outer normal to the cell C_i and $F|_{I_{ij}}$ represents the constant value of $F(W)$ at the interface ∂C_{ij}.

The flow is calculated by means of a numerical flux function, denoted Φ_{ij}:

$$\Phi_{ij} = \Phi_{ij}(W_i,W_j,\vec{n}_{ij}) = F|_{I_{ij}}\cdot\int_{\partial C_{ij}}\vec{n}_i\,d\gamma\,, \tag{3}$$

where $\vec{n}_{ij} = \displaystyle\int_{\partial C_{ij}}\vec{n}_i\,d\gamma$. The numerical flux function approximate the hyperbolic terms on the common boundary ∂C_{ij}. We notice that the computation of the convective fluxes is performed mono-dimensionnaly in the direction normal to the boundary of the finite volume cell. Therefore, the numerical calculation of the flux function Φ_{ij} at the interface ∂C_{ij} is achieved by the resolution of a one-dimensional Riemann problem in the direction of the normal $\vec{n}_{ij}$ by means of an approximate Riemann solver.

Several upwind numerical flux functions are available and could be formally written:

$$\Phi_{ij}(W_i,W_j,\vec{\nu}_{ij}) = \frac{F(W_i)+F(W_j)}{2}\cdot\vec{n}_{ij} + d\left(W_i,W_j,\vec{n}_{ij}\right)\,, \tag{4}$$

where the function $d\left(W_i,W_j,\vec{n}_{ij}\right)$ contains the upwind terms and depends on the chosen scheme. Here, we consider the HLLC Riemann solver, more details may be found in [4].

Such a formulation gives at best only a first-order scheme. However, a higher-order version could be achieved by employing the MUSCL technique.

2.2 Third-order accurate version

The MUSCL type reconstruction method is utilized to increase the order of accuracy of the scheme. This method was introduced by Van Leer in a series of papers, see for instance [12]. The idea is to use extrapolated values W_{ij} and W_{ji} of W at the interface ∂C_{ij} to evaluate the flux, cf. Figure 2. The following approximation is performed:

$$\Phi_{ij} = \Phi_{ij}(W_{ij}, W_{ji}, \vec{\nu}_{ij})\,,$$

with W_{ij} and W_{ji} which are linearly interpolated as:

$$\left\{ \begin{array}{rcl} W_{ij} & = & W_i + \dfrac{1}{2}\,(\nabla W)_{ij} \cdot \overrightarrow{P_iP_j}\,, \\ W_{ji} & = & W_j + \dfrac{1}{2}\,(\nabla W)_{ji} \cdot \overrightarrow{P_jP_i}\,. \end{array} \right. \tag{5}$$

where in contrast to the original MUSCL approach, the approximate "slopes" $(\nabla W)_{ij}$ and $(\nabla W)_{ji}$ are defined for any edge and obtained using a combination of centered and upwind gradients. Several types of gradients are available to define this slopes:

- *the nodal centered gradient* which is related to the edge P_iP_j and is defined as:

  $$(\nabla W)_{ij}^{C} \cdot \overrightarrow{P_iP_j} = W_j - W_i\,,$$

- *the nodal $P1$-Galerkin gradient* which is related to the cell C_i and is computed by averaging the gradients of all the tetrahedra containing the vertex P_i:

  $$(\nabla W)_{ij}^{M} = \frac{1}{aire(C_i)} \sum_{K \in C_i} \left(\frac{vol(K)}{4} \sum_{k \in K} (\nabla W)|_K \right)\,.$$

  where the tetrahedra gradients is $(\nabla W)|_K = \sum_{k\in K} W_k\, \nabla \phi_k|_K$, with $\phi_k|_K$ the $P1$ basis functions associated to vertex k on the tetrahedra K.

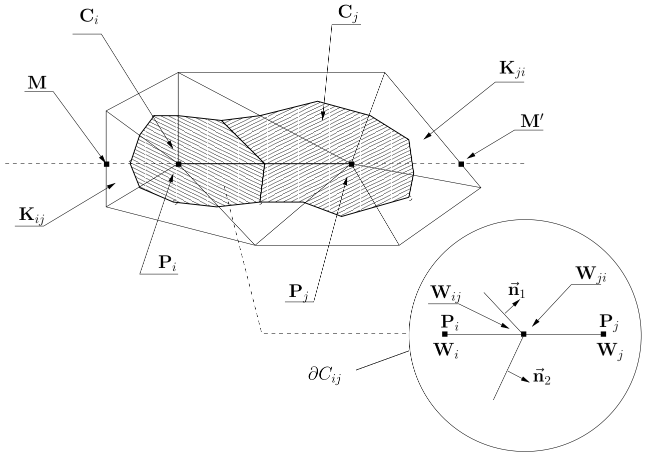

Figure 2: *Illustration of finite volume cells construction in two dimensions with two neighboring cells C_i and C_j, and the upwind triangles K_{ij} and K_{ji} associated to the edge P_iP_j. Definition of the common boundary ∂C_{ij} with the representation of the solution extrapolated values for the MSUCL type approach.*

- *the upwind gradient* which is also related to edge P_iP_j and is computed according to the definition of downstream and upstream tetrahedra of the edge P_iP_j denoted K_{ij} and K_{ji}, respectively (cf. Figure **??**). Then, upwind gradients could be defined for vertices P_i and P_j as:

$$(\nabla W)_{ij}^{D} = (\nabla W)|_{K_{ij}} \quad \text{and} \quad (\nabla W)_{ji}^{D} = (\nabla W)|_{K_{ji}} \,.$$

Consequently, parametrized nodal gradients could be build by introducing the β-scheme:

$$(\nabla W)_{ij} \cdot \overrightarrow{P_iP_j} = (1-\beta)(\nabla W)_{ij}^{C} \cdot \overrightarrow{P_iP_j} + \beta(\nabla W)_{ij}^{D} \cdot \overrightarrow{P_iP_j} \,,$$

where $\beta \in [0,1]$ is a parameter controlling the amount of upwinding, for instance the scheme is centered for $\beta = 0$ and fully upwind for $\beta = 1$. In our case, $\beta = 1/3$ is used which is the most accurate scheme. Indeed, it can be demonstrate that this scheme is third-order for the 2D linear advection on structured triangular meshes of Friedrichs-Keller type. This high-order gradient is denoted by: $(\nabla W)_{ij}^{HO} = 2/3\,(\nabla W)_{ij}^{C} + 1/3\,(\nabla W)_{ij}^{D}$.

2.3 Limiting function

The scheme resulting from the previous procedure is not monotone. Therefore, limiting functions are coupled with the previous gradient evaluation to guarantee TVD property to the scheme. The gradient of Relation (5) is substituted by a limited gradient denoted $(\nabla W)_{ij}^{lim}$. Here, we consider the three-entries limiter introduced by Dervieux which is a generalization of the Superbee limiter. We use the limiter defined by:

$$\begin{cases} Lim(u,v,w) & = 0 & \text{if } uv \leq 0\,, \\ Lim(u,v,w) & = Sign(u)\, min(2\,|u|, 2\,|v|, |w|) & \text{else.} \end{cases}$$

Practically, the entries are: $Lim((\nabla W)_{ij}^{C}, (\nabla W)_{ij}^{D}, (\nabla W)_{ij}^{HO})$.

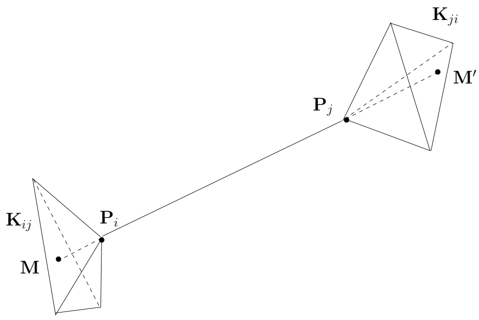

Figure 3: *Downstream K_{ij} and upstream K_{ji} tetrahedra associated to the edge $[P_i, P_j]$.*

2.4 Time advancing

An explicit scheme is used to advance the Euler equations in time by a line method, *i.e.,* time and space are treated separately. Once the equations have been discretized in space, a set of ordinary differential equations in time is obtained:

$$W_t - L(W) = 0\,.$$

To discretize the previous relation, a high-order multi-step Runge-Kutta scheme is considered. Such time discretization methods, called SSP (Strong-Stability-Preserving), have non linear stability properties which are particularly suitable for the integration of system of hyperbolic conservation laws where discontinuities appear. These schemes verify the TVD property.

The optimal 2-stage 2-order SSP Runge-Kutta scheme introduced by Shu and Osher [9] is the following modified Euler scheme:

$$\begin{aligned} W^{(1)} &= W^n + \Delta t\, L(W^n)\,, \\ W^{n+1} &= \frac{1}{2}W^n + \frac{1}{2}W^{(1)} + \frac{1}{2}\Delta t\, L(W^{(1)})\,, \end{aligned}$$

which accept to use a CFL coefficient up to 1.

In this study, we consider an extension of this 2-order SSPRK scheme with 5-stage given in [10] that allows us to consider CFL coefficient up to 4. This scheme reads:

$$\begin{aligned} W^{(1)} &= W^n + \frac{1}{4}\Delta t\, L(W^n)\,, \\ W^{(k)} &= W^{(k-1)} + \frac{1}{4}\Delta t\, L(W^{(k-1)}) \quad \text{for } k = 2\ldots 4\,, \\ W^{n+1} &= \frac{1}{5}W^n + \frac{4}{5}W^{(4)} + \frac{1}{5}\Delta t\, L(W^{(4)})\,, \end{aligned}$$

In practice, we consider a CFL coefficient equal to 3.5.

3 ANISOTROPIC MESH ADAPTATION

Mesh adaptation provides a way of controlling the accuracy of the numerical solution by modifying the domain discretization according to size and directional constraints. It is well known that mesh adaptation captures accurately shocks far form the aircraft in the computational domain while reducing significantly the cpu time [1]. Therefore, the near field solution computation is performed with mesh adaptation techniques in order to obtain a sufficient accurate solution far from the jet.

For stationary problems, the mesh adaptation scheme aims at finding a fixed point for the mesh-solution couple. In other words, the goal is to converge towards the stationary solution of the problem and similarly towards the corresponding invariant adapted mesh.

At each stage, a numerical solution is computed on the current mesh with the Euler flow solver and has to be analyzed by means of an error estimate. The considered error estimate, based on a bound of the interpolation error in L^∞ norm, is geometric (thus independent of the problem) and anisotropic [6]. An anisotropic metric field is then defined *via* this error estimate that translates the solution variations into elements sizes and directions by means of the Hessian of the solution which is computed by a double $\mathbf{L}^2$ projection. This metric will replace the Euclidean one to modified the scalar product that underlies the notion of distance used in mesh generation algorithms. Next, an adapted mesh is generated with respect to this metric where the aim is to generate a mesh such that all edges have a length of (or close to) one in the prescribed metric and such that all elements are almost regular. Such a mesh is called a *unit mesh*. Finally, the solution is linearly interpolated on the new mesh. This procedure is repeated until the convergence of the solution and of the mesh is achieved.

3.1 Metric construction

For each mesh element K, the anisotropic error interpolation bound involves the second derivatives of the variable u:

$$\| u - \Pi_h u \|_{\infty,K} \leq c_d \max_{x \in K} \max_{e \in E_K} \langle \vec{e},\, |H_u(x)|\, \vec{e} \rangle = \varepsilon_K \,, \tag{6}$$

where c_d is a constant related to the dimension, E_K is the set of edges of K and $|H_u| = \mathcal{R}|\Lambda|\mathcal{R}^{-1}$ is the absolute value of the Hessian of the variable u ($\mathcal{R}$ being the matrix of eigenvectors and $|\Lambda| = diag(|\lambda_i|)$ being the absolute value of the matrix of eigenvalues). The error estimate aims at defining a discrete metric field that prescribes size and stretching requirements for the mesh adaptation procedure.

A discrete metric approximation which uses the mesh vertices as support is considered. Let h_{min} and h_{max} be the minimal and the maximal mesh element size, respectively, and let ε be the desired interpolation error. Then, according to Relation (6), we define at each mesh vertex the anisotropic metric tensor $\mathcal{M}$ as:

$$\mathcal{M} = \mathcal{R}\,\tilde{\Lambda}\,\mathcal{R}^{-1}\,, \text{ where } \tilde{\Lambda} = diag(\tilde{\lambda_i}) \text{ and } \tilde{\lambda_i} = \min\left(\max\left(\frac{c\,|\lambda_i|}{\varepsilon}, \frac{1}{h_{max}^2}\right), \frac{1}{h_{min}^2}\right).$$

Introducing a minimal and a maximal element size is a practical way to avoid unrealistic metrics. It also allows us to control the time stepping in the flow solver.

Physical phenomena can involve large scale variations (e.g. multi-scale phenomena, recirculation, and weak and strong shocks). It is thus difficult to capture the weakest phenomena *via* mesh adaptation, and even harder to do it when, for instance in CFD, shocks are located in the flow. Capturing such weak phenomena is crucial for obtaining an accurate solution by taking into account all phenomena interactions in the main flow area. To this end, we suggest the following error estimate:

$$\left\| \frac{u - \Pi_h u}{\gamma |u|_\epsilon + (1-\gamma)\,\bar{h}\,\|\nabla u\|_2} \right\|_{\infty,K} \le c \max_{x \in K} \max_{\vec{e} \in E_K} \langle \vec{e}, \frac{|H_u(x)|}{\gamma |u(x)|_\epsilon + (1-\gamma)\,\bar{h}\,\|\nabla u(x)\|_2} \vec{e} \rangle \,, \quad (7)$$

where $\bar{h}$ is the diameter (*i.e.,* the length of its largest edge) of element K and γ is a parameter belongs to $[0,1]$ that will be considered close to zero if strong shocks are involved in the flow. Notice that γ will be chosen equal to 1 in the case of isotropic mesh adaptation.

3.2 Mesh adaptation

In our approach, the adaptation of the current mesh is based on the specification of a discrete anisotropic metric tensor at each vertex. For these purposes, the standard Euclidean scalar product is modified according to a proper metric tensor field $\mathcal{M}$. The aim is then to generate a mesh such that all edges have a length of (or close to) one in the prescribed metric and such that all elements are almost regular. Such a mesh is called a *unit mesh*. Let P be a vertex and let $\mathcal{M}(P)$ be the metric at P, the length of the edge PX with respect to $\mathcal{M}(P)$ is defined as:

$$l_{\mathcal{M}(P)}(PX) = \langle \overrightarrow{PX}\,,\, \overrightarrow{PX}\, \rangle^{\frac{1}{2}}_{\mathcal{M}(P)} = \sqrt{{}^t\overrightarrow{PX}\,\mathcal{M}(P)\,\overrightarrow{PX}}\,.$$

As the metric is not uniform over the domain, we need to consider the metrics at the edge endpoints as well as all intermediate metrics along the edge. To achieve this, we assume that an edge PX has a local parametrization $PX = P + t\overrightarrow{PX}$ and we introduce its average length as:

$$l_{\mathcal{M}}(\overrightarrow{PX}) = \int_0^1 \sqrt{{}^t\overrightarrow{PX}\,\mathcal{M}(P + t\overrightarrow{PX}\,)\,\overrightarrow{PX}}\; dt\,. \quad (8)$$

The volume mesh is adapted by local mesh modifications of the previous mesh (the mesh is not regenerated) using mesh operations: vertex insertion, edge and face swap, collapse and node displacement. The vertex insertion procedure uses an anisotropic generalization of the Delaunay kernel. Notice that here the gradation of the mesh (the size variation between two neighboring elements) is not controlled.

4 SONIC BOOM MODELING

The propagation code is a ray tracing algorithm based upon the waveform parameter method developed by Thomas [11]. It allows us to propagate the near field perturbations to the ground in order to get the sonic boom signature of the aircraft. In this approach, the pressure wave is characterized by three parameters:

- m_i the slope of pressure waveform segment i

- Δp_i the pressure rise across shock at the juncture of pressure waveform segment i and $i-1$
- λ_i the time duration of pressure waveform segment i.

A system of three ordinary differential equations (ODE), one for each parameter, is solved to propagate the pressure wave in the atmosphere:

$$\left\{\begin{array}{rcl} \dfrac{dm_i}{dt} &=& C_1\, m_i^2 + C_2\, m_i\,, \\[2ex] \dfrac{d\Delta p_i}{dt} &=& \dfrac{1}{2}\, C_1 \Delta p_i (m_i + m_{i-1}) + C_2 \Delta p_i\,, \\[2ex] \dfrac{d\lambda_i}{dt} &=& -\dfrac{1}{2}\, C_1 (\Delta p_i + \Delta p_{i+1}) - C_1 m_i \lambda_i\,, \end{array}\right. \tag{9}$$

with notations:

$$C_1 = \frac{\gamma+1}{2\gamma}\,\frac{a_0}{p_0 c_n} \quad \text{and} \quad C_2 = \frac{1}{2}\left(\frac{3}{a_0}\frac{da_0}{dt} + \frac{1}{\rho_0}\frac{d\rho_0}{dt} - \frac{2}{c_n}\frac{c_n}{dt} - \frac{1}{A}\frac{A}{dt}\right)\,,$$

where the index 0 design the air ambient quantities and where we denote by a the sound speed, ρ the density, c_n the speed that a wave propagates normal to itself and A the (acoustic) ray tube area as cut by the waveform. All these quantities are function of the altitude. The speed that a wave propagates normal to itself is given by $c_n = a_0 + \vec{V_0}.\vec{n}$ where $\vec{V_0}$ is the wind velocity and $\vec{n}$ the wavefront unit normal. If the wind velocity is assumed to be zero then we have $c_n = a_0$.

Acoustic rays are emitted by the aircraft and are orthogonal to wavefronts. They represent the paths along which the acoustic disturbance propagates. They form the *ray tube* or *ray cone*. The initial direction of a ray is given by the ray cone near the aircraft, orthogonal to the Mach cone. To compute the ray tube area, four rays are selected, separated by a time increment and an azimuthal increment. The initial directions of these rays are governed by the aircraft flight parameters and the azimuth. With that initial

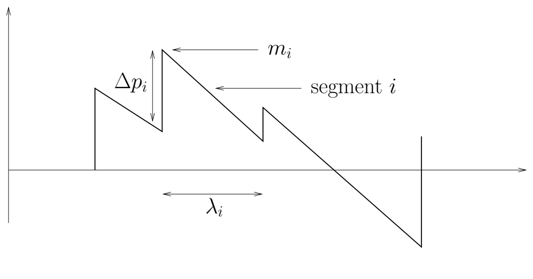

Figure 4: *Illustration of the three parameters m_i, Δp_i and λ_i characterizing the pressure wave.*

condition, ray shapes may be traced. Rays are traced by direct numerical integration of the eiconal. All four rays are traced in this way and ray tube area are computed by numeric differencing.

To evaluate these quantities, the atmosphere (i.e., the temperature and pressure evolution function of the altitude) needs to be define. Here, we use the no-wind ICAO Standard atmosphere [7]. This atmosphere may be accurately represented by the following analytical functions:

$$\begin{aligned} T(z) &= \max(T_{gnd} - 6.5\, z\,,\, 216.65)\,, \\ p(z) &= \left\{ \begin{array}{ll} p_{gnd} \left(1 - \dfrac{6.50\, z}{T_{gnd}}\right)^{5.26} & \text{if } 0\, km < z < 12.25\, km\,, \\ p_{gnd} \left(1 - \dfrac{3.04\, z}{T_{gnd}}\right)^{12.26} & \text{if } 12.25\, km < z < 30\, km\,, \end{array} \right. \end{aligned}$$

where $T_{gnd} = 288.15\,K$ and $p_{gnd} = 101,300\,Pa$ are the temperature in Kelvin and pressure in Pascal at the ground, respectively. Moreover, we assume that the air is following the perfect gas rule. A complementary hypothesis is made assuming that there is no-wind between the flight altitude and the ground.

To solve this system, we just have to integrate in time the three ordinary differential equations of System (9) by considering a sufficiently small time step in order to assume that the variable C_1 and C_2 are constants. Moreover, the time step must be adequately truncated throughout the resolution. Indeed, as the wave propagates down the ray path, shocks often will coalesce and new shocks will be formed. When this occurs one or more of the λ_i will go to zero. When one of the λ_i does go to zero somewhere between two points on the ray path, the associated segment is suppress and the waveform parameters must be redefined.

In this study, we only analyze sonic boom signature for an angle of emission (or azimuthal angle) of acoustical rays equal to zero. The ground reflexion is also taken into account by a reflexion coefficient equal to 1, thus implying pressure doubling at the ground surface (altitude 0) because of reflexion.

The solution of the ensemble is possible if the initial distribution of the variables is accessible. The near field solution of the Euler code is used as initialization. More precisely, the segments in our implementation correspond to a uniform *a posteriori* discretization along the flight path. The variables values on this discretization are obtained by interpolating the variables of the aerodynamic near field. In our approach, the segment discretization is finer than the one used in the CFD computation.

5 COUPLING BOTH MODELS

Let us first introduce some notations. We denote by α the angle of attack of the aircraft and β the Mach cone angle with the flow direction defined by $\sin\beta = M^{-1}$ where M is the

Mach number. Moreover, let L be the length of the aircraft and R be the distance of the observation point from the line parallel to the flow direction (or the ground) going through the nose of the aircraft. This distance form the aircraft is generally expressed with the ratio R/L. Finally, we denote by p the acoustical pressure and p_∞ the atmospherical pressure.

Due to the complexity of the phenomenon, the simulation of the sonic boom signal at the ground requires to couple CFD models and acoustic propagation equations. The pressure distribution obtained under the aircraft in the near field region is used to set up the initial conditions for the propagation of the acoustic wave to the ground. However, the modeled flow in the near field is three-dimensional and non linear in nature whereas the propagation is a linear one-dimensional model. Thus, the near field solution must be locally axi-symmetric where the pressure distribution is extracted to ensure a valid coupling. This is a necessary condition to take all the elements of the aircraft geometry (body, wings,...) into account.

According to the linear supersonic aerodynamic theory or the Whitham functions, the pressure variation $\frac{p(x)-p_\infty}{p_\infty}$ is decreasing in $\sqrt{R/L}$. Therefore, the near field solution is converged and considered locally axi-symmetric if we have a $\sqrt{R/L}$ decrease for the pressure variation. In other words, we haven't any more the presence of non-linear effect in the flow and the coupling become valid. Consequently, an accurate near field solution, obtained with mesh adaptation, is sufficiently far from the aircraft when the pressure variation decreases in $\sqrt{R/L}$ and could be used as initial condition for the the sonic boom prediction.

Now, we present our choice for the extraction line. Assuming that the aircraft is flying on the x-axis from positive to negative x, the extraction line at $R/L = 0$ is the line going through the nose of the aircraft with an angle of α in the symmetric plane Oxz, *i.e.,* a line parallel to the flow direction. This line is defined by its two extrema:

$$\left\{\begin{array}{lcl} x_0 &=& x_{jet} - l_{front}\, cos\,\alpha \\ y_0 &=& y_{jet} \\ z_0 &=& z_{jet} - l_{front}\, sin\,\alpha \end{array}\right. \qquad \text{and} \qquad \left\{\begin{array}{lcl} x_1 &=& x_{jet} + (L + l_{back})\, \cos\,\alpha \\ y_1 &=& y_{jet} \\ z_1 &=& z_{jet} + (L + l_{back})\, \sin\,\alpha \end{array}\right.$$

where $P_{jet} = (x_{jet}, y_{jet}, z_{jet})$ is the nose of the aircraft and l_{front} and l_{back} are the length of the line before the nose and after the tail of the aircraft, respectively. Then, we just translate the line along the Mach cones to define it at a given R/L as follow:

$$\left\{\begin{array}{lcl} x_i^{R/L} &=& x_i + R\,\dfrac{\cos(\beta-\alpha)}{\sin\,\beta} \\ y_i^{R/L} &=& y_i \\ z_i^{R/L} &=& z_i - R\,\dfrac{\sin(\beta-\alpha)}{\sin\,\beta} \end{array}\right. \qquad \text{for } i = 0, 1\,.$$

The extraction line is used as an initial input for the propagation code.

6 NUMERICAL RESULTS

We study a supersonic business jet (SSBJ) provided by Dassault Aviation (Figure 5, left) flying at a supersonic speed of 1.6 Mach with an angle of attack of 3 degrees at an altitude of $13,680$ meters ($45,000$ feet). The length of the SSBJ is 36 meters. The complete aircraft is included in a sphere with a diameter of 1 kilometer, cf. Figure 5, right.

The simulations have been carried out in serial on a Macintosh G5 with 2.5 GHz PowerPC processor and 2 GB of memory.

In order to define the desired accuracy of the simulation, we precise some physical and physiological aspect regarding the sonic boom.

The audible frequencies for a human body is situated between 20 Hz and 20 kHz with a maximal sensibility around 3 kHz. The corresponding wave lengths are given by $\lambda = a_0\, f^{-1}$. Therefore, we have $\lambda = 17$ m at 20 Hz, $\lambda = 1.7$ cm at 20 kHz and $\lambda = 10$ cm for 3 kHz.

If we consider an aircraft with length of 50 meters flying at Mach 1.6 with an atmosphere sound speed $a = 300$ m/s and a ground sound speed $a_0 = 340$ m/s, then the time duration of the sonic boom is almost 0.1 second. The rise time of such sonic boom is less than 1 millisecond (from experimental measurement) that correspond to a wave length of the order of 34 cm.

Consequently, this imply that wave length under 30 cm are filtered by absorption mechanism in the atmosphere. Thus, it is not necessary to describe the signal source with an accuracy too lower than this value. From this conclusion, in our adaptive simulations we consider a maximal precision of 30 cm.

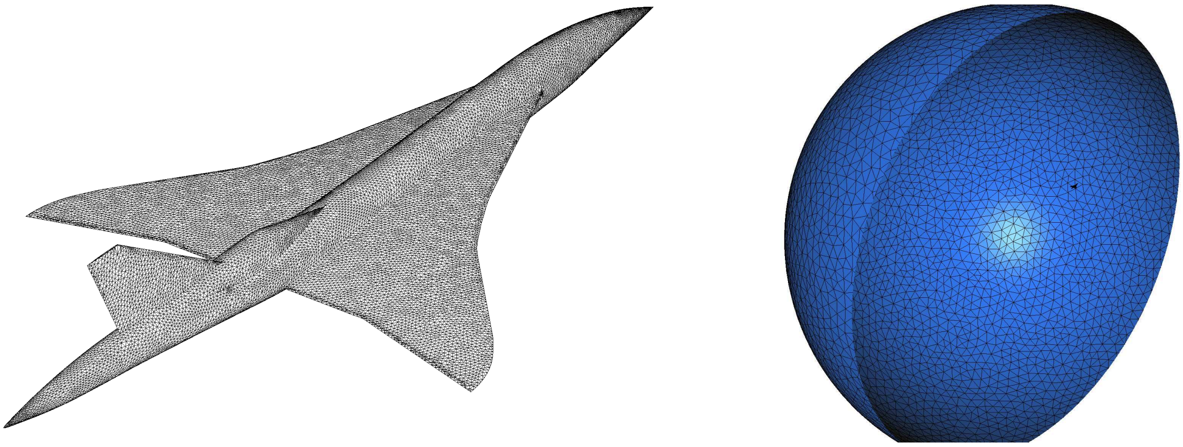

Figure 5: *Left, SSBJ's geometry represented by its surface mesh. Right, spherical computational domain with the SSBJ.*

6.1 Isotropic vs. anisotropic mesh adaptation.

A previous study has been done in [2] using isotropic mesh adaptation. The resulting adapted meshes, on the Mach number values, are shown in Figure 6. In this study, we were only able to propagate mesh refinement until almost $R/L = 0.75$ with a precision of 40 cm, after this distance shock waves are diffused and then the signal is lost. Notice that the presented isotropic adapted mesh contains almost $800,000$ vertices and 4.7 millions tetrahedra on a half domain (corresponding to a 1.6 millions vertices mesh on the whole domain). The conclusion of this study was that anisotropic mesh adaptation is mandatory.

Here, we present the results obtained with anisotropic mesh adaptation described in Section 3. We choose to control the error on the Mach number, as the number of Mach is really representative of the flow even if an accurate near field pressure distribution is required. A total number of 15 adaptations has been performed each 150 time steps of the flow solver and a maximal spatial resolution of 30 cm has been considered. The desired error, which appears in Relation 7, is chosen equal to 0.1 with the parameter γ set to 0.97.

The final anisotropic adapted mesh contains almost $700,000$ vertices and 4.1 millions tetrahedra. This mesh is shown in Figure 7 on the left. We notice that mesh refinement along Mach cones have been propagated farer than in the isotropic case but not in the whole domain, Figure 8 on the left. A deeper analyze shows that the near field signal is propagated accurately until $R/L = 2.5$ with twice times less vertices than the isotropic case, Figure 9 on the left. After, the signal start to be diffused and is completely lost at $R/L = 5$.

In Figure 9, left, the variations of $\sqrt{\frac{R}{L}}\,\frac{p(x)-p_\infty}{p_\infty}$ with R/L are presented. The first shock is converged but the rest of the signal still have some variation due to the non-linear

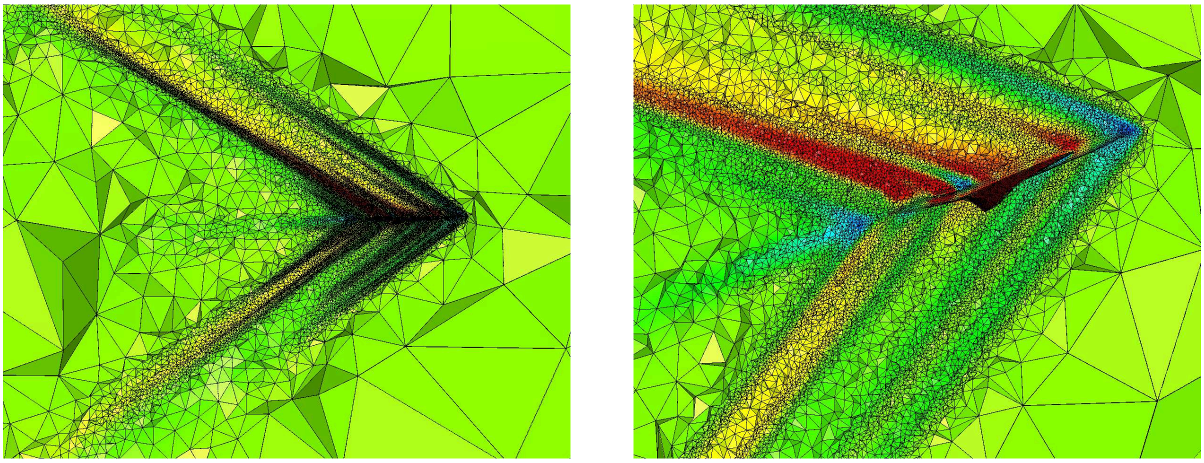

Figure 6: *Isotropic adapted mesh.*

effects and thus seems not to be completely converged. Indeed, the sonic boom signature shows that the same amplitude is obtained for the first shock, but some differences are present in rest of the signal, Figure 10, left.

In conclusion, the signal need to be farer propagated to be completely converged. This adaptive anisotropic approach is not sufficient.

6.2 A new anisotropic mesh adaptation approach

Recent progress on the theoretical background regarding the metric concept has been developed in [3], called continuous metric. This new approach define an optimal metric for minimizing the interpolation error in norm $\mathbf{L}^p$ in order to generate anisotropic adapted meshes. The choice of an L^p norm instead of the L^∞ norm could be crucial, indeed norms with lower p are able to capture weak variation of the solution.

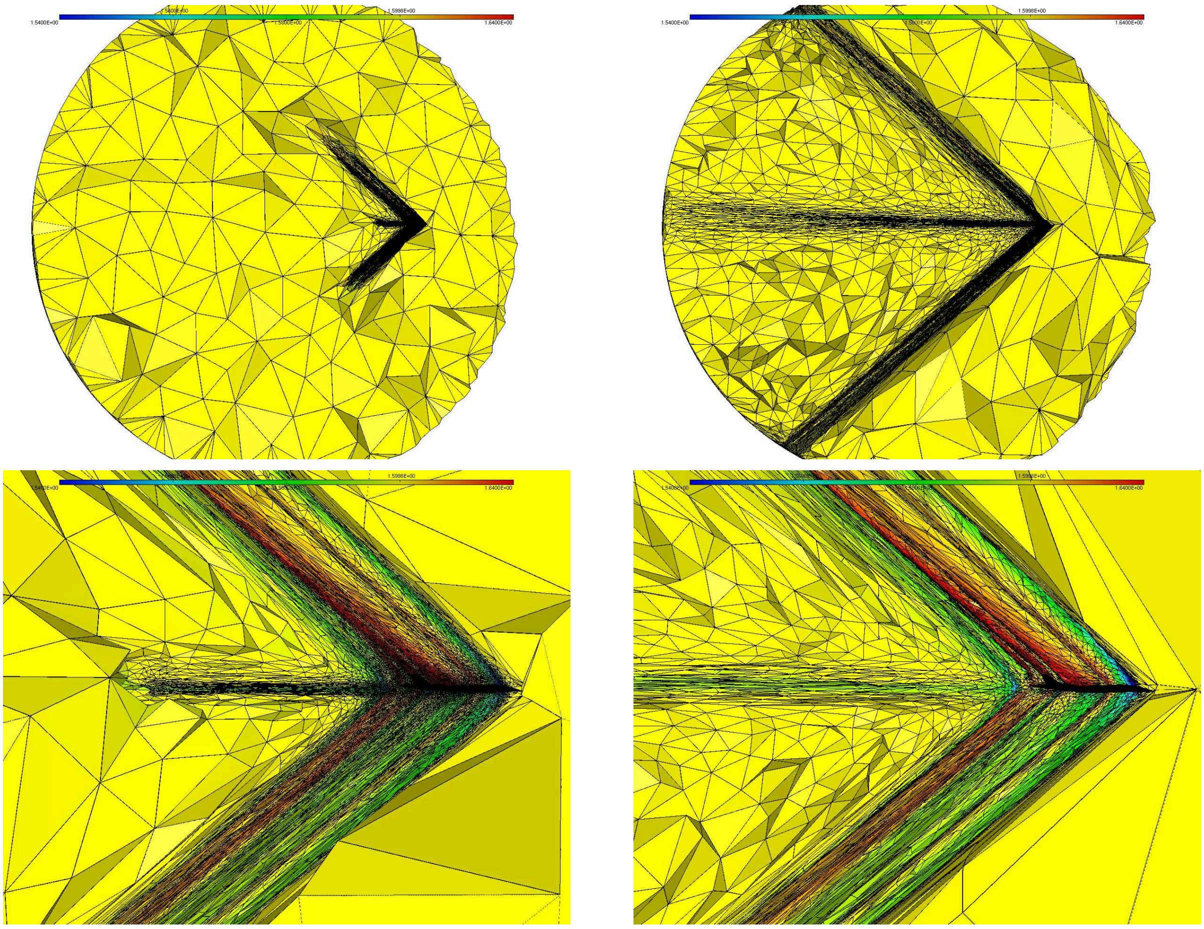

Figure 7: *Anisotropic adapted meshes. Left, classical anisotropic mesh adaptation. Right, anisotropic mesh adaptation with continuous metric.*

In consequence, here we consider the continuous metric controlling the $\mathbf{L}^2$-norm of the error defined by:

$$\mathcal{M}_{\mathbf{L}^2} = D_{\mathbf{L}^2} \left(\det |H_u|\right)^{-\frac{1}{7}} \mathcal{R}_u^{-1} \, |\Lambda| \, \mathcal{R}_u \quad \text{with} \quad D_{\mathbf{L}^2} = N^{\frac{2}{3}} \left(\int_\Omega \left| \prod_{i=1}^{3} \frac{\partial^2 u}{\partial {\alpha_i}^2} \right|^{\frac{2}{7}} \right)^{-\frac{2}{3}} . \qquad (10)$$

No normalization relation are considered.

As previously, we choose to control the error on the Mach number and a total number of 15 adaptations has been performed each 150 time steps of the flow solver. In this new approach, no maximal resolution is considered, we try to obtain the best mesh controlling the error in $\mathbf{L}^2$-norm with $600,000$ vertices.

The final adapted anisotropic mesh contains almost $570,000$ vertices and 3.3 millions tetrahedra This mesh is shown in Figure 7 on the right. In this case, mesh adaptation has been performed in whole computational domain We notice that the solution, e.g. Mach cones, has been propagated in the whole domain, Figure 8 on the right.

A more precise analysis shows that the near field signal is propagated accurately until $R/L = 6.5$ with less vertices than the previous approach, Figure 9 on the right. After, the signal is slightly diffused but the signal is still well represented.

The signal between $R/L = 4$ and $R/L = 6.5$ seems to be almost converged, the variations of $\sqrt{\frac{R}{L}} \frac{p(x)-p_\infty}{p_\infty}$ with R/L are presented in Figure 9, right. This is emphasized on sonic boom signature were almost the same signal is obtained for R/L between 4 and 6.5, Figure 10, right.

In conclusion, for this geometry the signal seems to be converged around $R/L = 5$ with an accuracy of $600,000$ vertices.

7 CONCLUSIONS

An accurate sonic boom modeling, coupling CFD near field simulation and ray tracing algorithm for the far field, has been presented. A crucial point was the use of an adequate anisotropic mesh adaptation approach in order to have a valid coupling by propagating the near field signal far enough from the aircraft.

This approach was able to propagate anisotropic mesh refinement in whole computational domain without any difficulties to preserve the solution accuracy. It has been demonstrated numerically that, in this case, a near field extraction at $R/L = 5$ seems to be adequate to obtain a precise sonic boom signature.

However, some points still have to be analyzed such as the chosen precision for the near field. Is this spatial precision enough to get an accurate sonic boom signature ? A more complex geometry including for instance nacelles may emits more non-linear effects and therefore is a farer propagation needed ?

Moreover, some diffusive effect were pointed out for the flow solver. A less diffusive MUSCL approach presented in [5] will be more adequate.

REFERENCES

[1] F. Alauzet, *Adaptation de maillage anisotrope en trois dimensions. Application aux simulations instationnaires en Mécanique des Fluides*, (in French), Thèse de Doctorat de l'Université Montpellier II, 2003.

[2] F. Alauzet and B. Mohammadi, Optimisation 3D du nez d'un SuperSonic Business Jet basée sur l'adaptation de maillages. Application à la réduction du bang sonique, (in French), *INRIA RR-5053*, (2003).

[3] F. Alauzet, A. Loseille, A. Dervieux and P.J. Frey, Multi-Dimensional Continuous Metric for Mesh Adaptation, *Proc. of 15th Int. Meshing Roundtable*, Birmingham, AL, USA, 2006.

[4] P. Batten and N. Clarke and C. Lambert and D.M. Causon, On the choice of wavespeeds for the HLLC Riemann solver, *SIAM J. Sci. Comput.*, **18** (6), 1553–1570, (1997).

[5] C. Debiez and A. Dervieux, Mixed-element-volume MUSCL methods with weak viscosity for steady and unsteady flow calculations, *Computer & Fluids*, **29**, 89–118, (2000).

[6] P.J. Frey and F. Alauzet, Anisotropic mesh adaptation for CFD computations, *Comput. Methods Appl. Mech. Engrg.*, **194**, 5068–5082, (2005).

[7] ICAO, *Manual of the ICAO Standard Atmosphere (extended to 80 kilometres)*, Doc 7488 - Third Edition, (1993).

[8] K.J. Plotkin, Review of sonic boom theory, *AIAA paper*, 89-1105, (1989).

[9] C.W. Shu and S. Osher, Efficient implementation of essentially non-oscillatory shock-capturing schemes, *J. Comput. Phys.*, **77**, 439–471, (1988).

[10] R.J. Spiteri and S.J. Ruuth, A new class of optimal high-order strong-stability-preserving time discretization methods, *SIAM J. Numer. Anal.*, **40** (2), 469–491, (2002).

[11] Ch. Thomas, Extrapolation of sonic boom pressure signatures by the waveform parameter method, *Nasa TN. D-6832*, (1972).

[12] B. Van Leer, Towards the ultimate conservative difference scheme I. The quest of monotonicity, *Lecture notes in physics*, **18**, p. 163, (1972).

[13] G. B. Whitham, The flow pattern of a supersonic projectile, *Comm. Pure Appl. Math.*, **5**, 301–348, (1952).

[14] G. B. Whitham, *Linear and Nonlinear waves*, Wiley/Interscience, New York, (1974).

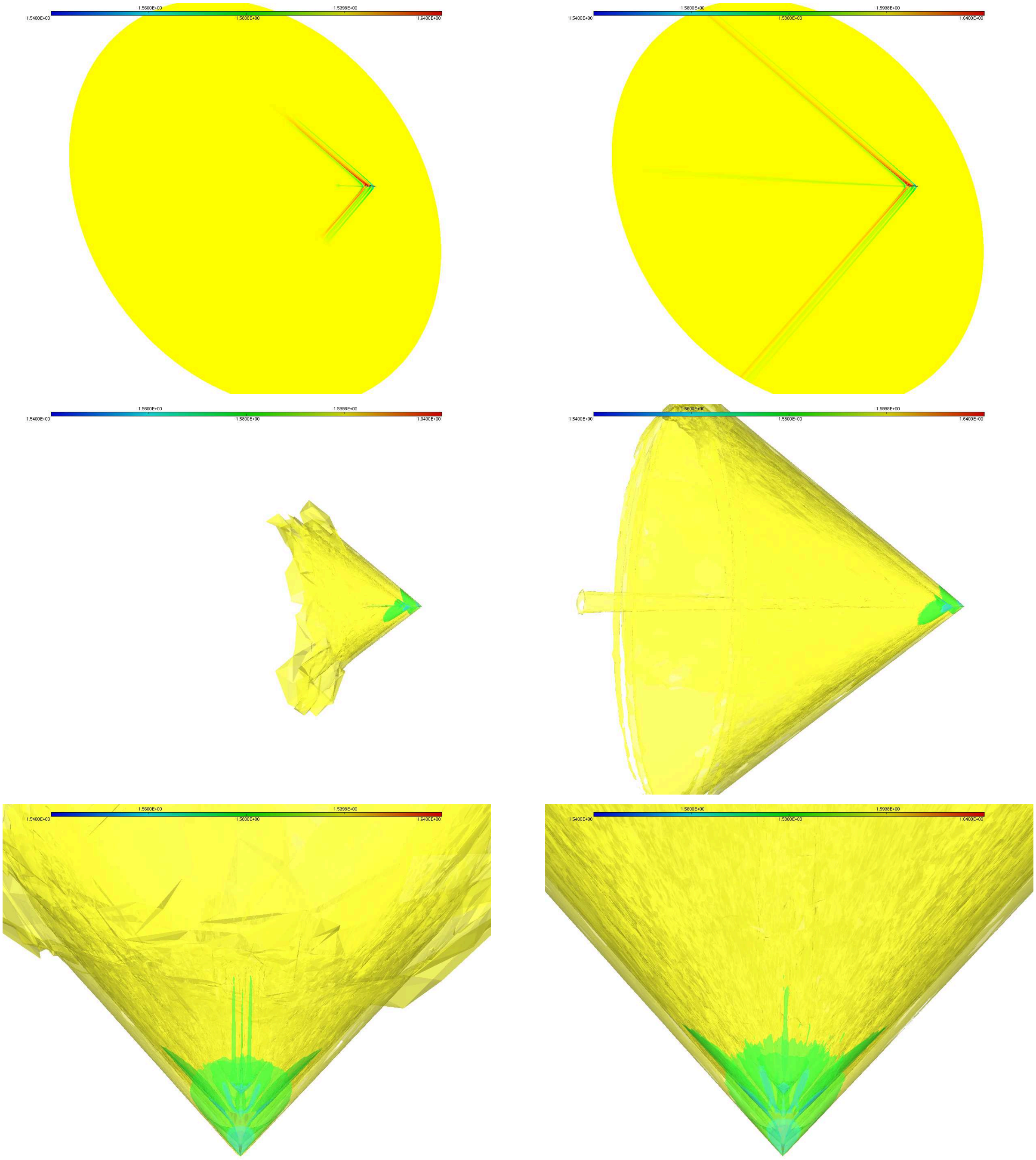

Figure 8: *Mach number iso-value in a plane (top) and Mach number iso-surface (middle and bottom) for the anisotropic mesh adaptations. Left, classical anisotropic mesh adaptation. Right, anisotropic mesh adaptation with continuous metric.*

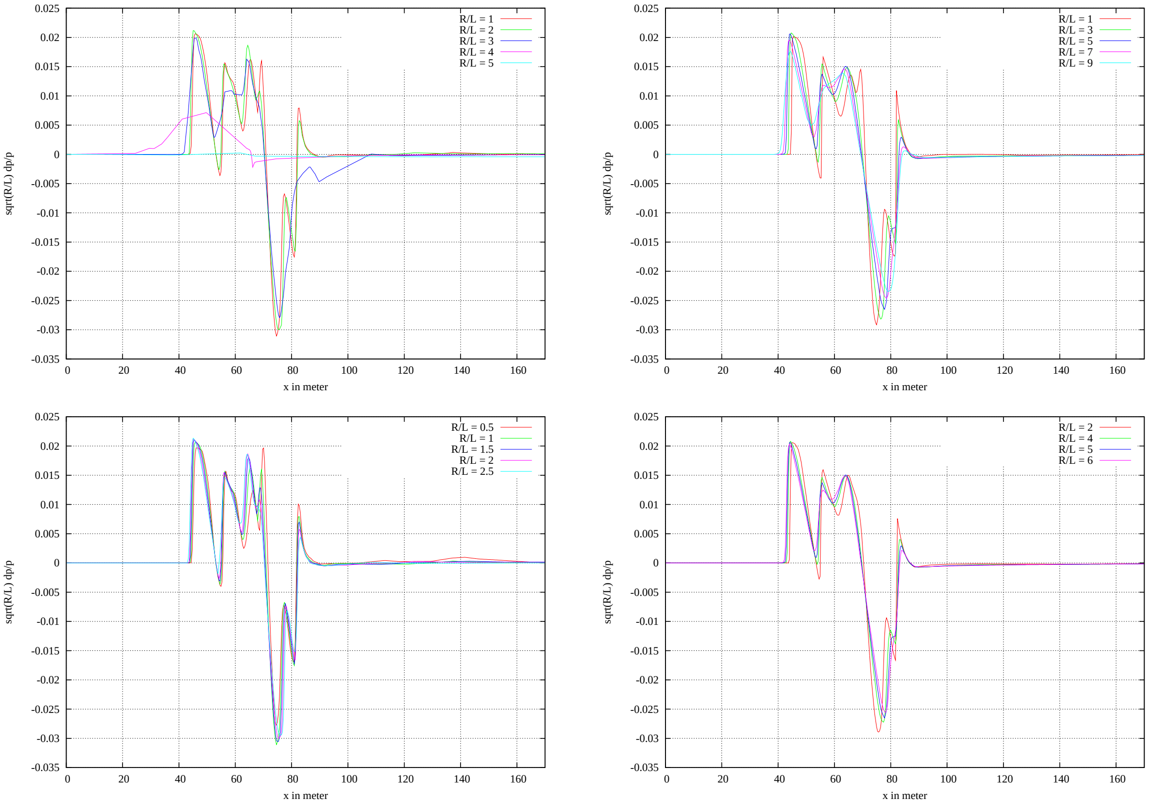

Figure 9: *Near field signature extracted from several R/L. Left, classical anisotropic mesh adaptation. Right, anisotropic mesh adaptation with continuous metric.*

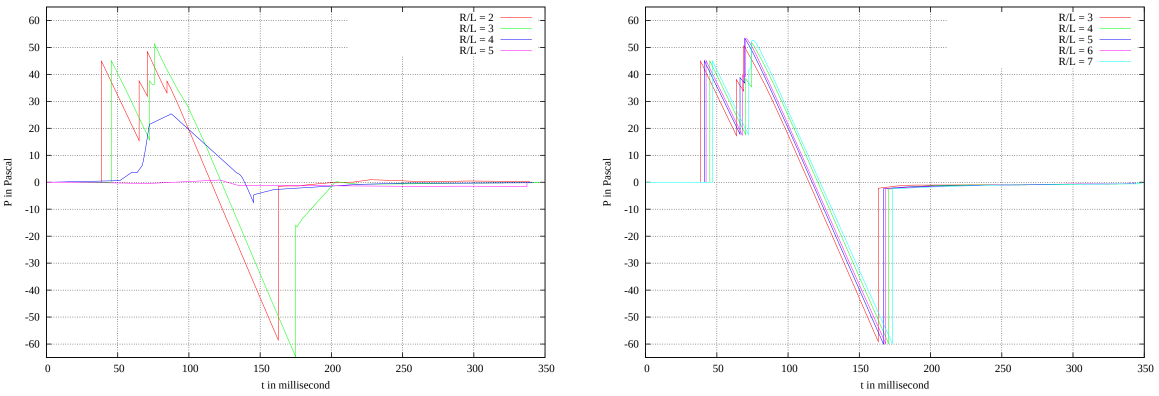

Figure 10: *Sonic boom signature obtained from different R/L near field initializations. Left, classical anisotropic mesh adaptation. Right, anisotropic mesh adaptation with continuous metric.*